

A broad-band spectral analysis of eight radio loud type 1 AGN selected in the hard X-ray band

M. Molina,¹ L. Bassani,² A. Malizia,² A.J. Bird,¹ A.J. Dean,¹ M. Fiocchi,³ F. Panessa,³

A. De Rosa,³ R. Landi²

¹*School of Physics and Astronomy, University of Southampton, SO17 1BJ, Southampton, U.K.,*

²*IASF/INAF, via Gobetti 101, I-40129 Bologna, Italy,*

³*IASF/INAF, via Fosso del Cavaliere 100, I-00133 Rome, Italy*

ABSTRACT

Starting from a complete sample of type I AGN observed by *INTEGRAL* in the 20–40 keV band, we have selected a set of 8 AGN which can be classified as radio loud objects according to their 1.4 GHz power density, radio to hard X-ray flux density ratio and radio morphology. The sample contains 6 Broad Line Radio Galaxies and 2 candidate ones. Most of the objects in our sample display a double lobe morphology, both on small and large scales. For all the objects, we present broad-band (1–110 keV) spectral analysis using *INTEGRAL* observations together with archival *XMM-Newton*, *Chandra*, *Swift/XRT* and *Swift/BAT* data. We constrain the primary continuum (photon index and cut-off energy), intrinsic absorption and reprocessing features (iron line and reflection) in most of the objects. The sources analysed here show remarkable similarities to radio quiet type I AGN with respect to most of the parameters analysed; we only find marginal evidence for weaker reprocessing features in our objects compared to their radio quiet counterparts. Similarly we do not find any correlation between the spectral parameters studied and the source core dominance or radio to 20–100 keV flux density ratios, suggesting that what makes our objects radio loud has no effect on their high energy characteristics.

Key words: Galaxies – AGN – Radio – X-rays – Gamma-rays.

1 INTRODUCTION

Most of what is known about Active Galactic Nuclei (AGN) is essentially based on studies of radio quiet sources, which make up almost 90% of the entire AGN population. It is now widely accepted that active galaxies are powered by accretion onto a supermassive black hole: the observed radiation, spanning the entire electromagnetic spectrum, is produced by a cold accretion disk and by a hot corona, as proposed in the so-called two-phase model (Maraschi & Haardt 1997). In the X-ray domain, the emission of radio quiet Broad Line AGN (Seyfert 1) is, to the first order, well described by a power law of photon index 1.8–2.0, extending from a few keV to over 100 keV; at higher energies there is evidence for an exponential cut-off, the exact value of which is still uncertain (Perola et al. 2002; Risaliti 2002). Secondary features such as the Fe $K\alpha$ line and the Compton reflection component are also commonly observed; they are considered to be the effects of reprocessing of the primary continuum and are relatively well understood (Mushotzky et al. 1993). Studies performed on samples of Broad Line Radio Galaxies (BLRG from now on; Sambruna et al. 1999; Grandi et al. 2006) have shown that these objects show optical/UV continuum and emission line characteristics similar to their radio

quiet counterparts, but display some fundamental differences in their X-ray behaviour. BLRG, in fact, exhibit flatter/harder power law slopes than radio quiet Seyfert 1 galaxies and are also known to have weaker reprocessing features (e.g. Sambruna et al. 1999 and Grandi et al. 2006). The origin of these differences is however far from being understood. A possible cause for the observed diversity could be ascribed to a different disk geometry and/or accretion flow efficiencies, or to the presence of jets and beaming effects that contaminate/dilute the AGN component and the reprocessing features; ionised reflection, which naturally produces weaker reflection features, has also been considered in the literature (Ballantyne, Ross & Fabian 2002). Now that a large sample of AGN detected above 20 keV by *INTEGRAL* is available, it is possible and important to perform a comparison between different classes of AGN, by measuring the shape of the primary continuum together with the high energy cut-off and the reflection component. In the present work we focus on the broad-band (1–110 keV) spectral analysis of a sample of eight radio loud type 1 AGN, combining *XMM-Newton*, *Chandra*, *Swift/XRT* and *BAT* data together with *INTEGRAL/ISGRI* measurements. We also compare our results to a sample of radio quiet Seyfert 1s detected by *INTEGRAL*

and recently studied by Panessa et al. (2008) and finally discuss the implications of our findings.

2 THE SAMPLE

The definition of radio loudness is rather vague, with different criteria applied in the literature (see Zamfir, Sulentic & Marziani 2008 for a critical discussion). Traditionally, empirical boundaries were set by the radio power density at 5 GHz ($P_{5\text{GHz}}$; Miller, Peacock & Mead 1990) and the radio (at the same frequency) to optical B band flux density ratio (R_B ; Kellerman et al. 1989); according to these boundaries, an AGN is radio loud if $P_{5\text{GHz}} \geq 10^{32} \text{ erg s}^{-1} \text{ Hz}^{-1}$ and $\text{Log}(R_B) \geq 1$. In time, different surrogate definitions of both parameters have appeared in the literature involving radio data at different frequencies and comparison with even UV and X-ray fluxes to deal with objects selected in bands other than the optical. More recently Zamfir, Sulentic & Marziani (2008) suggested the use of the source radio morphology as a further criterion to divide radio loud from radio quiet objects. Since FR I morphology is quite rare in broad line radio loud AGN, while double-lobe FR II appearance is much more common, these authors suggest the adoption of this last morphology as a further discriminator, i.e. FR II-like objects are by default radio loud. We therefore selected our radio loud AGN on the basis of similar criteria: the power density at 1.4 GHz ($P_{1.4\text{GHz}}$), the radio (at the same frequency) to the 20-100 keV flux density ratio (R_{HX}) and the source morphology, again at 1.4 GHz. Sources were selected from a set of 35 Broad Line (BL) galaxies extracted from a complete sample of *INTEGRAL* detected AGN¹. Because many of these objects are newly discovered, it is difficult to have information for all of them at 5 GHz and/or in the B band, hence the use of the more ready available 1.4 GHz and 20-100 keV data. 1.4 GHz information has been obtained from the HEASARC database² for 29 objects in the sample, except in the case of IGR J13109-5552, where the 1.4 GHz flux was extrapolated using the 4.85 and 0.83 GHz fluxes available in the HEASARC radio catalogues. *INTEGRAL* data were derived from the fluxes reported in Bird et al. (2007; see also table 1A) and are available for all objects in the sample. Candidate radio loud objects were selected on the basis of their location in the diagram shown in figure 1, where the radio quiet/loud boundaries on both axes are set by the weakest FR II source in our sample, i.e. IGR J21247+5058. This source has been fully discussed by Molina et al. (2007) and it is now a well established case of a radio loud AGN on the basis of various arguments. In particular it has been classified as an FR II galaxy by Molina et al. (2007) with a $L_{5\text{GHz}} \sim 10^{31} \text{ erg s}^{-1} \text{ Hz}^{-1}$, an order of magnitude lower than the traditional limit, making this source one of the weakest FR II galaxies reported to date.

By means of these boundaries we identified 8 radio loud AGN: QSO B0241+62, B3 0309+411, 3C 111, 3C 390.3, IGR J13109-5552, 4C 74.26, S5 2116+81 and IGR J21247+5058 (see table 1); note the ambiguous location of two additional objects, Markarian 6 and MCG+08-11-11, which are below the adopted boundaries but very close to IGR J21247+5058. Information at 5 GHz and in

the B band are available for all these sources so that a cross-check can be made on their radio power density and radio-to-optical flux density ratio according to the more conventional definition used by Miller, Peacock & Mead (1990) and Kellerman et al. (1989). Both values are listed in table 1 for all 8 candidates plus Markarian 6 and MCG+08-11-011, which we keep under consideration due to their location in figure 1. 5 AGN have $P_{5\text{GHz}} \geq 10^{32} \text{ erg s}^{-1} \text{ Hz}^{-1}$ and in any case all but Markarian 6 and MCG+08-11-011 have a 5 GHz power density exceeding that of IGR J21247+5058. All the objects, including Mrk 6 and MCG+08-11-011, have $\text{Log}(R_B) \geq 1$; note that in IGR J21247+5058, R_B cannot be estimated due to the lack of information on the B magnitude.

Next we examined the radio morphology of all our 8 radio loud candidate AGN, plus again Mrk 6 and MCG+08-11-011 (see table 1). All but 2 sources (i.e. QSO B0241+62 and IGR J13109-5552) are well known Broad Line Radio Galaxies (see table 1 and NED, Ballantyne 2005 and Molina et al. 2007) and show a morphology with two lobes extending from the central nucleus (see for example NVSS contour maps available in NED); the extension of the lobes for B3 0309+411 and 4C 74.26 is more than 1 Mpc, hence their classification as giant radio galaxies (de Bruyn 1989; Riley et al. 1988). These double-lobed objects are classified in the literature as FR II galaxies, with the exception of 4C 74.26 and S5 2116+81, which still have an uncertain/unknown nature. QSO B0241+62 and IGR J13109-5552 have been poorly studied at radio frequencies and their classification is uncertain; both are Seyfert I according to NED and Masetti et al. 2008. QSO B0241+62, shows a compact unresolved core in the NVSS map, although high resolution radio imaging indicates a possible double-lobe morphology within this core structure (Tzanetakakis et al. 1978). The sky region containing IGR J13109-5552 has not been mapped by the NVSS, but the source is present in the Molonglo Galactic Plane Survey 2nd Epoch (MGPS-2) Compact Source Catalogue (Murphy et al. 2007); a cut-off image of the source shows an unresolved but elongated structure. QSO B0241+62 is reported as a relatively strong source in various radio surveys, has a flat radio spectrum with a $\alpha \sim 0.1$ ³ (Vollmer et al. 2005) and so almost certainly qualifies as a radio loud AGN. IGR J13109-5552 has less information at radio frequencies but the few available data provide a flat spectrum also in this case ($\alpha \sim 0.3$).

We also checked, for completeness, the morphology of Markarian 6 and MCG+08-11-011 in the NVSS/NED database: both are similar to QSO B0241+62, i.e. display a compact core which, at higher resolution, reveals a clear (in Markarian 6; Kharb et al. 2006) or possible (in MCG+08-11-011; Ulvestad & Wilson 1986) double lobe structure. However their radio spectra are steeper ($\alpha \sim 0.6-0.7$; Vollmer et al. 2005) than in the previous two cases and more similar to radio quiet AGN. This evidence, coupled with their lower radio power argues against a classification as radio loud AGN and therefore both objects are not considered further.

Table 1A lists all relevant information on the 8 sources chosen for this study, including redshift, Galactic column density in their direction, 20-100 keV flux and luminosity and the 5/8 GHz radio core dominance (CD). The Galactic column densities are taken from Dickey & Lockman (1991), while the parameter $CD = S_{\text{core}} / (S_{\text{tot}} - S_{\text{core}})$ is taken from Fan & Zhang (2003); the only exceptions are B3 0309+411 and IGR J21247+5058, for which the CD parameter has been evaluated using data from

¹ This sample extracted from the 3rd IBIS/ISGRI catalogue (Bird et al. 2007; Malizia et al. 2008) contains all AGN detected with a significance greater than 5.5σ in the 20-40 keV band and having $z \leq 0.14$; it contains 35 type 1 objects, 30 type 2 sources, 3 Narrow Line Seyfert 1s, and 7 Blazars/QSOs

² <http://heasarc.gsfc.nasa.gov/>

³ $S_{\nu} \propto \nu^{-\alpha}$

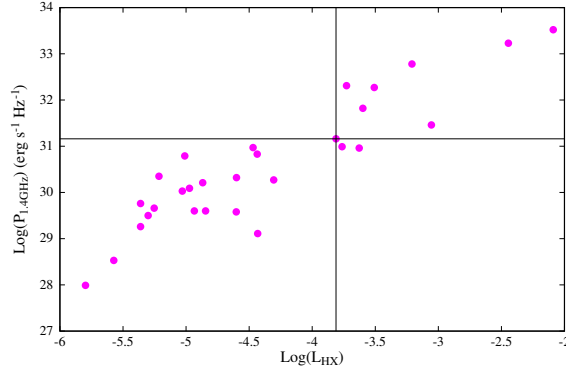


Figure 1. 1.4 GHz power density versus the 1.4 GHz to 20-100 keV flux density ratio for most sources in the *INTEGRAL* BL AGN catalogue. The boundaries on both axis are set by the values of the weakest FR II in the sample (IGR J21247+5058) and are defined by the lines drawn in the figure.

Table 1

Candidate Radio Loud AGN			
Name	Type	$\text{Log}(P_{5\text{GHz}})$ $\text{erg s}^{-1}\text{Hz}^{-1}$	$\text{Log}(R_B)$
QSO B0241+62	-	31.230	2.8-2.9
B3 0309+411	BLRG, FR II?	32.322	3.3
3C 111	BLRG, FR II	31.919	4.4-5.0
IGR J13109-5552	-	31.929	2.7
3C 390.3	BLRG, FR II	32.477	3.7
4C 74.26	BLRG, FR I/FR II	31.939	1.9-2.0
S5 2116+81	BLRG, FR?	31.771	1.9
IGR J21247+5058	BLRG, FR II	31.041	-
MCG+08-11-011	-	29.886	1.6
Mrk 6	-	29.934	1.5-1.8

Ishwara-Chandra & Saikia (1999) and Molina et al. (2007) respectively. No information on CD is available for IGR J13109-5552.

The radio core dominance spans a large range of values from 0.04 to 1.9. Sources with high values of this parameter are those in which the beamed radio emission is emitted in a direction closer to the line of sight; in these sources, jet emission is likely to play a greater role than in sources with smaller values of CD . Contrary to expectations, we do not find any convincing correlation between CD and either $(P_{1.4\text{GHz}})$ or R_{HX} , indicating that in at least some of our sources a jet component alone cannot be the origin of the source radio loudness. As a final remark, we point out that our 8 radio loud sources make up around 20% of the 20-40 keV complete sample of BL active galaxies and are therefore a non-negligible fraction of the *INTEGRAL* AGN population.

3 DATA REDUCTION

The sources in our sample have all been observed by *XMM-Newton* with the exceptions of QSO B0241+62, for which *Chandra* data are available, and IGR J13109-5552 and S5 2116+81, for which *Swift/XRT* data have instead been used. MOS and pn (Strüder et al. 2001; Turner et al. 2001) data were reprocessed using the *XMM-Newton* Standard Analysis Software (SAS) version 7.0 employing the latest available calibration files. Only patterns corresponding to single, double, triple and quadruple X-ray events for the two MOS cameras were selected ($\text{PATTERN} \leq 12$), while for the pn only single and double events ($\text{PATTERN} \leq 4$) were taken into account; the standard selection filter $\text{FLAG}=0$ was applied. Observations have been filtered for periods of high background and the resulting exposures are listed in table 2. Source counts were extracted

from circular regions of typically $40''$ - $50''$ of radius centered on the source, while background spectra were extracted from circular regions close to the source or from source-free regions of typically $20''$ radius. The ancillary response matrices (ARFs) and the detector response matrices (RMFs) were generated using the *XMM-SAS* tasks *arfgen* and *rmfgen*; spectral channels were rebinned in order to achieve a minimum of 20 counts per each bin. For sources affected by pile-up (3C 111, 4C 74.26 and 3C 390.3) the central $5''$ of the PSF have been excised and spectra have been extracted from annular regions of typically $50''$ external radius. *XRT* data reduction for IGR J13109-5552 and S5 2116+81 was performed using the *XRTDAS* v1.8.0 standard data pipeline package (*xrtpipeline* v. 0.10.3) in order to produce screened event files. All data were collected in the Photon Counting (PC) mode (Hill et al. 2004), adopting the standard grade filtering (0-12 for PC) according to the *XRT* nomenclature. Source data have been extracted using photons in a circular region of radius $20''$; background data have been taken from various uncontaminated regions near the X-ray source, using either a circular region of different radius or an annulus surrounding the source.

Chandra data reduction for QSO B0241+62 was performed with CIAO 3.4 and CALDB 3.2.4 to apply the latest gain corrections. Subsequent filtering on event grade and exclusion of periods with high background resulted in a total exposure of 34 ks. The CIAO script “psextract” was used to generate the source spectrum, with its appropriate background and response files; spectral data were extracted from a circular region of radius $\sim 4''$ while background files were generated using a region of $\sim 18''$ in diameter. With a count rate of 0.14 counts/frame, the pile-up fraction is insignificant ($< 10\%$).

The *INTEGRAL* data reported here consist of several pointings

Table 1A

Source Data							
Name	RA	Dec	z	N_H^{gal} 10^{22} cm^{-2}	$F_{20-100 \text{ keV}}$ $10^{-11} \text{ erg cm}^{-2} \text{ s}^{-1}$	$L_{20-100 \text{ keV}}$ $10^{44} \text{ erg s}^{-1}$	CD [‡]
QSO B0241+62	41.285	+62.480	0.044	0.75	6.34	2.63	1.94
B3 0309+411	48.273	+41.343	0.136	0.13	2.57	9.75	1.17
3C 111	64.573	+38.014	0.0485	0.32	9.46	4.75	0.04
IGR J13109-5552v	197.682	-55.863	0.085	0.22	2.42	0.33	-
3C 390.3	280.586	+79.781	0.0561	0.04	6.06	4.06	0.09
4C 74.26	310.585	+75.145	0.104	0.12	4.87	10.97	0.95
S5 2116+81	318.492	+82.072	0.084	0.07	4.06	6.02	1.78
IGR J21247+5058	321.172	+50.972	0.02	1.11	10.90	0.94	0.76

‡: radio core dominance at 5 GHz, except for B3 0309+411B for which it is measured at 8 GHz (see references in the text).

performed by the *IBIS/ISGRI* (Ubertini et al. 2003; Lebrun et al. 2003) instrument between revolutions 12 and 429, i.e. the period from launch to the end of April 2006. *ISGRI* images for each available pointing were generated in various energy bands using the ISDC offline scientific analysis software OSA (Goldwurm et al. 2003) version 5.1. Count rates at the position of the source were extracted from individual images in order to provide light curves in various energy bands; from these light curves, average fluxes were then extracted and combined to produce an average source spectrum (see Bird et al. 2007 for details). Analysis was performed in the 20-110 keV band. In the present analysis we also made use of public *Swift/BAT* spectra, retrieved on the web⁴; spectra are from the first 9 months of operations of the *Swift/BAT* telescope (Baumgartner et al. 2008).

Table 2 reports the observation log of each source, i.e. the observation date of each X-ray observation and the exposure time for each instrument employed in the spectral analysis, with the exception of *Swift/BAT*.

4 BROAD-BAND SPECTRAL ANALYSIS

The *XMM-Newton*, *Chandra* and *Swift/XRT* data were fitted together with *INTEGRAL/ISGRI* and *Swift/BAT* data using XSPEC v.11.2.3 (Arnaud 1996); errors are quoted at 90% confidence level for one parameter of interest ($\Delta\chi^2=2.71$). In the fitting procedure, a multiplicative constant, C , has been introduced to take into account possible cross-calibration mismatches between the X-ray and the soft gamma-ray data. When treating the *INTEGRAL* data, this constant C_1 has been found to be close to 1 with respect to *XMM-Newton*, *Swift/XRT* and *Chandra* using various source typologies (Landi et al. 2007; De Rosa et al. 2008; Masetti et al. 2007; Panessa et al. 2008), so that significant deviation from this value can be confidently ascribed to source flux variability; also when considering *BAT* data, a cross-calibration constant C_2 different to 1 often means flux variation in the source analysed (see for example Ajello et al. 2008 and Winter et al. 2008). We also introduced cross calibration constants between the XMM instruments, pn/MOS1 and MOS2/MOS1; these were left free to vary and always found to be in the range 0.97-1.04. In all our fits, Galactic absorption (see table 1A) has already been taken into account so that any column densities reported in subsequent tables refer to absorption intrinsic to the source.

4.1 Towards a first approximation of the broad-band continuum.

We firstly fitted the broad-band data in the 0.5-110 keV energy range employing a simple power law (absorbed only by Galactic column density) in order to identify typical features of the AGN spectra. Some of our objects show evidence of excess counts below 1 keV; however, since the study of the soft excess is not the main objective of the present work, but rather the understanding of the high energy emission characteristics (photon index, high energy cut-off and reflection), we have focussed the analysis in the 1-110 keV energy range. Starting from the simple power law we introduced various spectral features such as intrinsic absorption and iron line, each time performing an F-test to verify the statistical significance of each new component and to provide a basic model able to describe the data at least to a first approximation (see table 3 and residuals with respect to this model in figures 2, 3, 4 and 5).

Inspection of figure 4 (left panel) suggests that the model employed in table 3 does not provide a good description of the data of 3C 390.3, where the residuals have an unusual concave shape, which may be due to the presence of a low energy component (soft excess) still affecting the spectrum around 2-3 keV. To take this into account we have added an extra feature to the model in the form of another power law or a blackbody component: both fits provide an equally significant improvement (typically more than 99%) and more acceptable residuals. The blackbody temperature is slightly higher than typically observed in Seyfert 1 galaxies (Panessa et al. 2008). It is interesting to note that so far no soft excess has been reported for this source except for an old claim never confirmed afterwards (Grandi et al. 1999); however a *Chandra* image of 3C 390.3 reveals extended soft X-ray emission around the nucleus so the soft excess photons we detect could be related to this component (Kadler et al. 2004 and figure 7 in Hardcastle & Croston 2005). We also point out that this source is known to have a variable column density, as found by Grandi et al. (1999); however in our analysis we were not able to detect any absorption in excess to the Galactic one. Due to the evidence found, in the following we adopt the model $w_a * w_a * (bb+po+zga)$ (table 3A and figure 6 right panel) as our basic representation of 3C 390.3.

It is also evident from table 3 and figure 5 (right panel) that IGR J21247+5058, has a very flat power law slope and consequently shows a mismatch between X-ray and soft gamma-ray data. It is however known from the literature that this source requires a model that takes into account complex absorption (Molina et al. 2007) in the form of two layers of material partially covering the central source. Hence, in the case of IGR J21247+5058, the simple intrinsic photoelectric absorption has been substituted by two partial covering components ($w_a * pc.fabs * pc.fabs * (po+zga)$ in XSPEC, see results in table 3B); when this model is applied, the

⁴ <http://swift.gsfc.nasa.gov/docs/swift/results/bs9mon/>

Table 2

Observations Log						
Name	Obs. Date	Exposure (pn) (sec)	Exposure (MOS) (sec)	Exposure (<i>XRT</i>) (sec)	Exposure (<i>Chandra</i>) (sec)	Exposure (<i>INTEGRAL</i>) [†] (sec)
QSO B0241+62	06-07/04/2001	-	-	-	34000	371986
B3 0309+411	04/09/2005	10990.1	19703.1/16138.6	-	-	506677
3C 111	14/03/2001	14542.1	76262.3/7116.3	-	-	200566
IGR J13109-5552	25/12/2006	-	-	6.58	-	1288
3C 390.3	08/10/2004	38762.3	32450.7/34603.9	-	-	305807
4C 74.26	06/02/2004	25643.5	28960.4/28960.4	-	-	121316
S5 2116+81	25/06/2006	-	-	5111.4	-	198462
	17/10/2006	-	-	5237.4	-	-
IGR J21247+5058	06/11/2005	22166	24245/23614	-	-	1067000

[†]: note that for *INTEGRAL* the exposure refer to a number of pointings in the period between launch and April 2006.

power law index becomes steeper and the X-ray/gamma-ray match is more acceptable (see figure 6 left panel).

Using the results reported in table 3, 3A and 3B we can already draw some conclusions, as the models employed at this stage provide, to a first approximation, a good description of the broad-band spectra of all our sources. In all but 2 AGN (B3 0309+411 and 3C 390.3), an intrinsic absorption component is strongly required by the data, at more than 90% confidence level for IGR J13109-5552 and S5 2116+81 and at more than 99% confidence level for the remaining objects. Note, however, that in 3C 111 the measured absorption could be due to a molecular cloud located between us and the source (Unger et al. 1985) and not intrinsic to the AGN. It is also interesting to note that only one out of eight objects displays complex absorption; a similar fraction was found in a sample of 9 radio quiet Seyfert 1 galaxies discussed by Panessa et al. (2008), where at least two objects required one or two layers of cold material partially obscuring the central nucleus.

The Fe K α line is detected in all the sources (99% confidence level), except in IGR J13109-5552 and S5 2116+81, but this may be due to *XRT* not being sensitive enough to detect the cold iron line around 6.4 keV. The line is narrow in all of our sources (hence the line width has been fixed to 10 eV), except in 4C 74.26, in which a quite strong and possibly broad iron line is detected (see also Ballantyne 2005 and Larsson et al. 2008). The line equivalent widths (EW) are found to be $\lesssim 100$ eV in all of our AGN. In two sources, namely 3C 111 and IGR J21247+5058, the equivalent width values are close to the capability limits of moderate resolution CCD instruments like *XMM-Newton*, calling for some caution in distinguishing between a real feature or just local noise. If the line is related to reflection, the observed values would imply a low reflection component parameter ($R=\Omega/2\pi$): in this case one may expect to find the EW to R ratio of the order of 100-130 eV (Perola et al. 2002) and consequently values of $R \leq 1$. We will come back to this point later.

Finally a note on the cross-calibration constants between the X-ray data and *IBIS/BAT* points: in some sources these constants are not consistent with 1, indicating, as expected, flux variations between the X-ray snap-shot observations and the time-averaged high energy spectral data.

4.2 Incidence of the high energy cut-off.

We next introduced a high energy cut-off in the primary power law of our basic model (see tables 4, 4A and 4B for model description in each source case). Only two of the eight sources in the sample strongly (at more than 99% confidence level) require a cut-off energy, i.e. 3C 111 and IGR J21247+5058; the cut-off is localised at

around 100 keV for 3C 111 and 80 keV for IGR J21247+5058. As far as the other sources are concerned, we could only set a lower limit for their cut-off energies at around 60-80 keV, apart from 3C 390.3, where the high energy cut-off could not be constrained at all. It is also interesting to note that the values of C_1 and C_2 tend to be higher when a cut-off energy component is added to the simple power law.

4.3 Incidence of the reflection component.

We then introduced reflection in our basic model of tables 3, 3A and 3B to verify the incidence of this spectral component in our broad-band data (again refer to tables 5, 5A and 5B for model description in each source case). We substituted the power law with the *pexrav* model in XSPEC, fixing the inclination angle at 30° (i.e. a nearly face-on geometry as expected in type 1 AGN) and the cut-off energy at 10000 keV. Taking into consideration the fact that the iron line EW is always $\lesssim 100$ eV, we assume that the reflection parameter R cannot have very high values; for this reason we initially allowed the reflection component to vary in the range 0-2. B3 0309+411 and 4C 74.26 require reflection at more than 99% confidence level, while 3C 390.3 and QSO B0241+62 at a lower confidence level (98% and 92% respectively). The reflection component is also significantly required (at more than 99% confidence level) in 3C 111 and IGR J21247+5058, the two AGN which also have a high energy cut-off; since in these two objects the iron line is very weak or possibly even absent we expect to observe negligible or low reflection and we thus suspect that a better fit is achieved when both R and E_{cut} are left free to vary (see next section). In S5 2116+81 and IGR J13109-5552 the data only provide a loose lower limit on R , likely due to the low statistical quality of the X-ray data.

The reflection values are all above 0.1 and, when constrained, are typically around 1. Despite being highly required, R is unconstrained in B3 0309+411 due to the upper bound of 2 set on the reflection; when this bound is removed, R is found to be $2.44^{+1.41}_{-1.17}$ and the constant becomes $C_2=2.30^{+1.10}_{-0.94}$. It is also important to note that R tends to be higher than predicted from the measured iron line EW and that the *pexrav* model provides, as expected, smaller values of C_1 and C_2 with respect to the previous two models.

4.4 Constraining both reflection and cut-off.

Finally, the broad-band spectra have been fitted with a cut-off power law reflected from neutral material (*pexrav* model but with E_{cut} free to vary, see table 6 and figures 7, 8 and 9 for model description in each source case). We removed IGR J13109-5552 and S5 2116+81 from the sample, as in both sources the quality of the

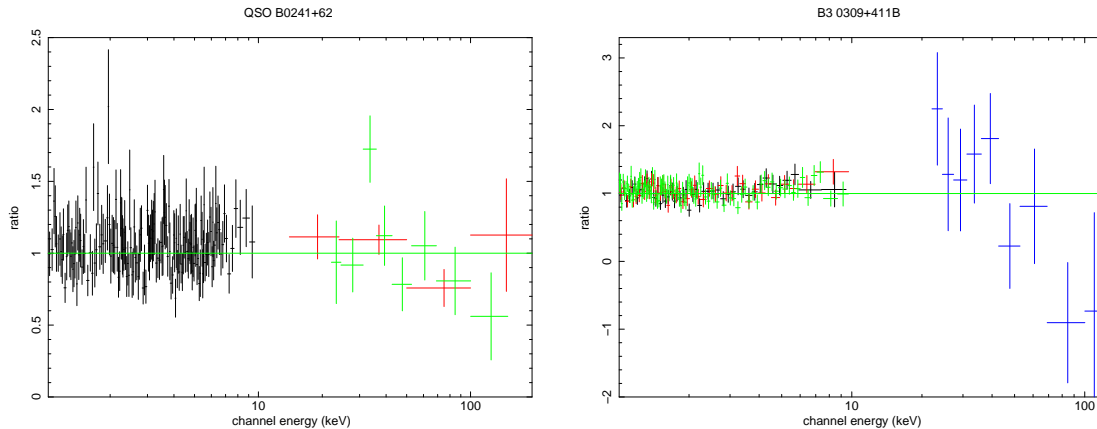


Figure 2. Model to data ratios for QSO B0241+62 (left panel) and B3 0309+411B (right panel). The model employed is a simple power law absorbed by both Galactic and intrinsic column density (only in the case of QSO B0241+62) plus a narrow Gaussian line component (see Table 3).

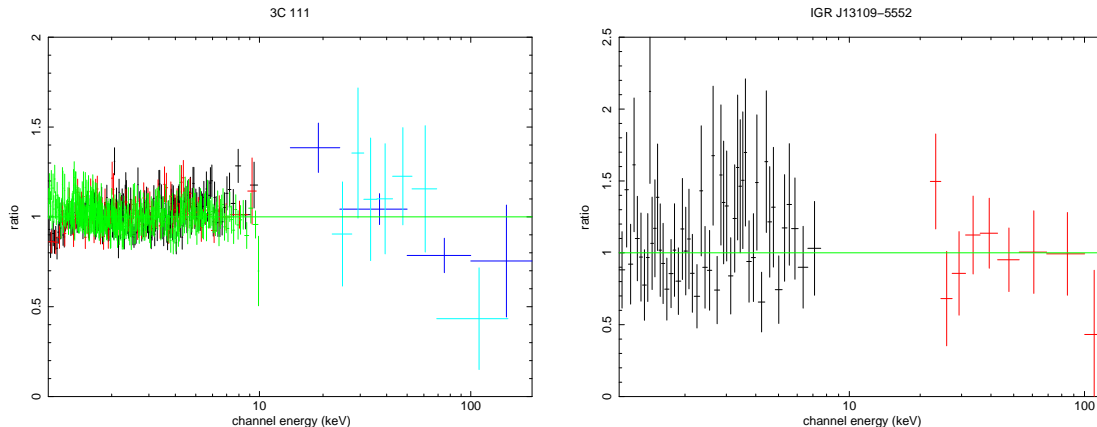


Figure 3. Model to data ratios for 3C 111 (left panel) and IGR J13109-5552 (right panel). The model employed is a simple power law absorbed by both Galactic and intrinsic column density plus, in the case of 3C111, a narrow Gaussian line component (see Table 3).

data allows no more complex fits than a simple power law (as in figure 10). Because in B3 0309+411 the reflection parameter exceeds the value of 2, we raised the upper bound on R . Although this model does not always provide a significant improvement with respect to previous fits, it nevertheless allows a simultaneous estimate of R and E_{cut} . We found that the reflection parameters of 5 objects and the cut-off energy of 4 are well constrained; in the cases of B3 0309+411, 3C 111 and IGR J21247+5058, these represent the best fit results. Due to the above considerations, we employ in the following discussion the values reported in table 6, with the eventual use of the upper limits on R and E_{cut} obtained for IGR J13109-5552 and S5 2116+81. It is important to note that the values of the parameters listed in table 6 are similar to those obtained in previous fits and also that in most sources the cross-calibration constants are now compatible with 1, an indication that the model is appropriate and that variability is not strong or common at high energies (see also Beckmann et al. 2007).

5 COMPARISON WITH PREVIOUS MEASUREMENTS

Five out of eight sources in our sample have been previously studied over a broad energy range similar to ours, so that a direct comparison is possible. Overall, we find that our parameter values are in good agreement, or compatible within errors, with those found by these previous works. In the case of 3C 111, all observations

point to a small reflection and a compatibly low iron line EW (Grandi et al. 2006; Lewis et al. 2005); our study yields a slightly higher value of R which is however still compatible, within errors, with previous results. We were able to put a stringent constraint on the high energy cut-off which we locate at a slightly lower value than in previous works, although well within the uncertainties found for example by *BeppoSAX* (Grandi et al. 2006).

Comparison of our results for 3C 390.3 with the works by Grandi et al. (1999) and Gliozzi et al. (2003) indicates good agreement on the cut-off energy, although we, as Gliozzi et al., could not place a constraint on this parameter, which is instead found by Grandi and collaborators to be around 250 keV, i.e. still compatible with our lower limit of 300 keV. Our value of the reflection parameter is also fully compatible with the result obtained using *BeppoSAX* data (Grandi et al. 1999), but higher (although compatible within relative uncertainties) than that obtained with RXTE spectra (Gliozzi et al. 2003).

We also find very good agreement with previous works for 4C 74.26 (e.g. Ballantyne & Fabian 2005, Grandi et al. 2006 and Larsson et al. 2008), even though we find a slightly lower cut-off energy value. Not much can be said about S5 2116+81 because of the poor statistical quality of our data; however, comparison with *BeppoSAX* data shows that our values do not contradict those found by Grandi et al. (2006).

Finally our results are in full agreement with a previous anal-

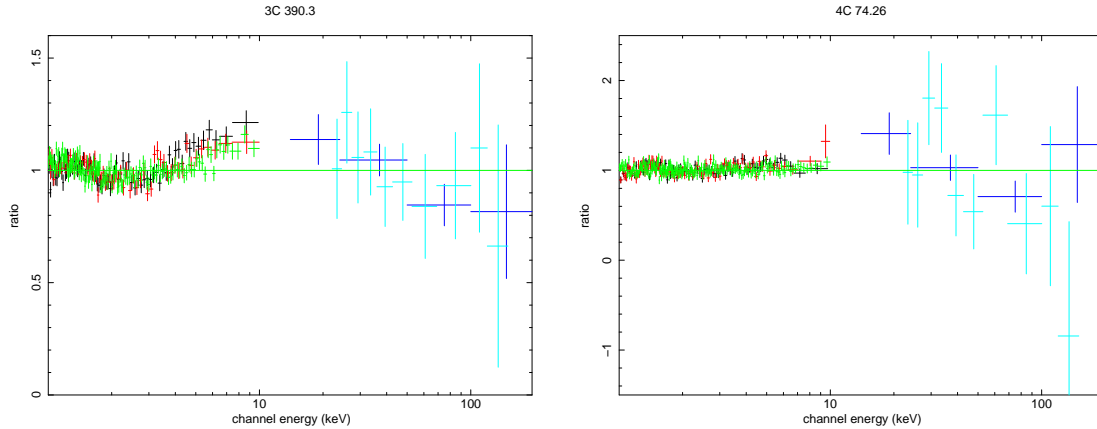


Figure 4. Model to data ratios for 3C 390.3 (left panel) and 4C 74.26 (right panel). The model employed is a simple power law absorbed by both Galactic and intrinsic column density (only in the case of 4C 74.26) plus a narrow (3C 390.3) or broad (4C 74.26) Gaussian line component (see Table 3).

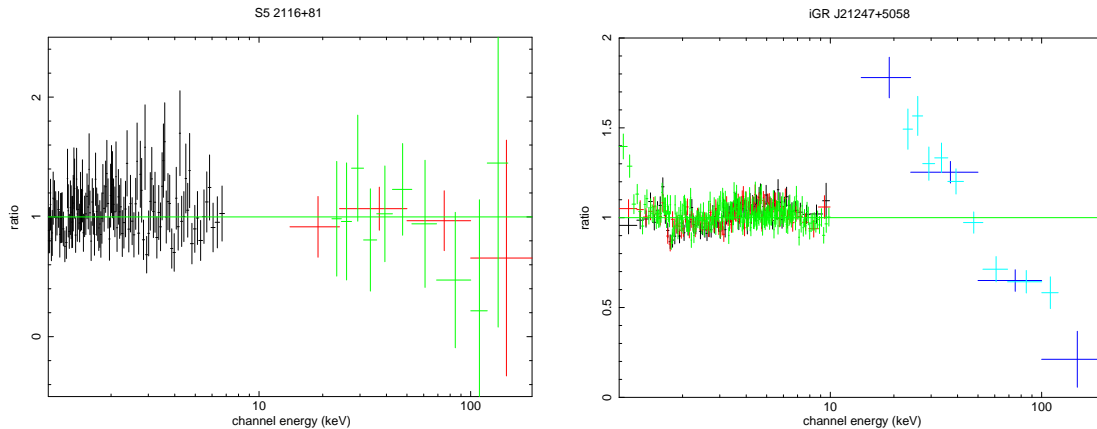


Figure 5. Model to data ratios for S5 2116+81 (left panel) and IGR J21247+5058 (right panel). The model employed is a simple power law absorbed by both Galactic and intrinsic column density plus, in the case of IGR J21247+5058, a narrow Gaussian line component (see Table 3).

ysis of X-ray/*INTEGRAL* data of IGR J21247+5058 (Molina et al. 2007). For QSO B0241+62, B3 0309+411 and IGR J13109-5552 no previous work is available and thus the analysis presented here is the first broad-band study for those 3 AGN.

6 DISCUSSION AND CONCLUSIONS

In the following we discuss the distribution of the fit parameters in our sample of AGN (see table 6) in comparison to a similar study made on a set of 9 radio quiet Seyfert 1 (Panessa et al. 2008) also detected by *INTEGRAL*. The power law slopes are found to be similar in both samples, i.e. around 1.5-2.0; only one of the radio bright AGN (the one requiring complex absorption) shows a flat power law continuum, while low values of Γ are more numerous in the sample of Panessa et al. (2008). The intrinsic absorption measured in our sources is generally small or absent ($\lesssim 2 \times 10^{21}$ atoms cm^{-2}), except for 3C 111 and IGR J21247+5058, and also similar to the values found for radio quiet type 1 AGN; in 3C 111 the extra absorption is probably due to intervening material between us and the source, while in the case of IGR J21247+5058 complex absorption is strongly required by the data. It is interesting to note that similar complexity, i.e. one or more layers of cold material partially covering the central nucleus, is also observed in 2 of the 9 objects studied by Panessa et al. (2008). We also point out that, up to very recently,

the only other BLRG known to have a similar spectral complexity regarding the absorption was 3C 445 (Sambruna et al. 2007), for which three layers of cold material were required to model the spectrum. Our analysis suggests that objects with complex absorption are present within the population of broad line AGN, independent of them being radio quiet or radio loud. Grandi et al. (2006) found evidence in their data for a correlation between absorption and radio core dominance, with more absorbed objects showing lower CD values. We do not find such a trend; furthermore we do not have any indication of a correlation between photon index or absorption and R_{HX} using both our sources and the radio quiet Seyferts of Panessa et al. (2008).

From the spectral analysis presented here, it is also evident that the high energy cut-off (although not required by all the sources in the sample) spans a wide range of values from ~ 40 keV up to more than 300 keV, as already found for radio quiet AGN (see for instance Molina et al. 2006 and Panessa et al. 2008). We also explored the possibility of a correlation between the high energy cut-off and the photon index but found nothing; a trend of increasing cut-off energy with higher Γ has been reported in the literature (see for instance Perola et al. 2002), but due to the strong dependency between these two parameters in the fitting procedure, it is difficult to discriminate between any true correlation and induced effects.

As far as the reflection fraction is concerned, we find in all but two cases (namely B3 0309+411 and 4C 74.26) very low values

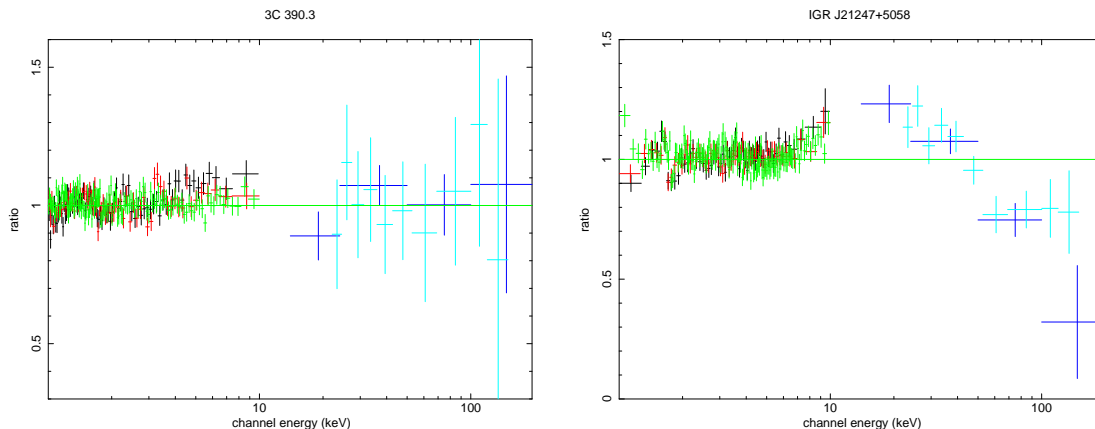


Figure 6. Model to data ratio for 3C 390.3 (left panel) and IGR J21247+5058 (right panel). The model used for 3C 390.3 is a simple power law absorbed by Galactic column density plus a blackbody component to model the soft excess and a narrow Gaussian line component (Table 3A). For IGR J21247+5058 the model used is instead a simple power law absorbed by Galactic column density and two layers of cold absorbing material partially covering the central source plus a narrow Gaussian line component (Table 3B).

for this component, typically below 1; as expected in these sources, the EW of the iron line is $\lesssim 100$ eV. Indeed if the iron line emission is associated with the optically thick material of the disk, one would expect the line EW to correlate with the reflection fraction as observed. However, in B3 0309+411 and 4C 74.26 the observed iron line EW is too small for the reflection measured: a possible explanation resides in the scatter expected in the EW values due to a variation in the iron abundance, or to a possible anisotropy of the source seed photons which might affect the observed spectrum (Petrucci et al. 2001; Merloni et al. 2006). For a given value of R , the EW could also differ according to the value of the power law photon index: up to $\Gamma=2$ the EW decreases as the spectrum steepens, while above $\Gamma=2$ the trend is reversed (Perola et al. 2002; Mattson, Weaver and Reynolds 2007). B3 0309+411 and 4C 74.26 both have steep spectra and so a lower EW than expected on the basis of the measured R value is not a surprise.

Overall we can conclude that, as already observed by a number of authors (i.e. Grandi et al. 2006 and Sambruna et al. 1999), the reprocessing features of the radio loud AGN analysed here tend to be, on average, quite weak. For a better comparison with their radio quiet counterparts, we have again used our data in combination with those of Panessa et al. (2008). Figure 11 shows a plot of R vs. EW for the entire sample. It is evident that radio loud AGN are more confined to a region of the plot characterized by low values of EW and to a lesser extent of R , whereas radio quiet objects tend to be more spread over both axes. This evidence does not seem to be related to the radio core dominance, suggesting that any dilution of the reprocessing features, at least for the sources reported here, is not caused by the presence of a jet. Since the observed difference is not striking, an accretion flow origin for the X/gamma-ray emission is a likely explanation for the production of the reprocessing features in our radio loud AGN; this agrees well with some of them being classified as FR II sources, i.e. the BLRG most closely resembling radio quiet AGN (Evans et al. 2006). Within this scenario, it is still possible that a different geometry and/or accretion flow efficiency involving the disk provides the condition for weaker reflection components in BLRG. Alternatively weaker reflection features might be the result of reprocessing in an ionised accretion disk, as suggested by Ballantyne, Ross & Fabian (2002); this would alleviate the need for a change in the accretion disk ge-

ometry and provide a more similar environment for both radio loud and radio quiet AGN.

Our sample is of course very small, limited to sources which have a small dynamic range of parameters (redshift, loudness, core dominance, etc.), and contains two objects (i.e. QSO B0241+62 and IGR J13109-5552) which deserve further radio studies and are not immediately confirmed as BLRG. We hope in the near future to improve the statistics, adding newly discovered AGN selected in the hard X-ray band in order to verify our findings as well as our novel approach of selecting radio loud type 1 sources.

ACKNOWLEDGEMENTS

We acknowledge the University of Southampton for financial support (M.M.) and the Italian Space Agency (ASI) financial and programmatic support via contracts I/008/07/0 and I/088/06/0. M. Molina wishes to thank V.A. McBride (Southampton University) for reducing *Chandra* data for QSO B0241+62.

REFERENCES

- Ajello M., Rau A., Greiner J. et al. 2008, *ApJ*, 673, 96
- Arnaud K. A. 1996, *Astronomical Data Analysis Software and Systems V*, eds Jacoby G. and Barnes J., p.17, ASP Conf Series vol. 101
- Ballantyne, D. R., Ross, R. R., Fabian, A. C. 2002, *MNRAS*, 332, 45
- Ballantyne D.R. 2005, *MNRAS*, 362, 1183
- Ballantyne D.R. & Fabian A.C. 2005, *ApJ*, 622, 97
- Baumgartner W., Tueller J., Mushotzky R. et al. 2008, *ATel* 1429.
- Beckmann V., Barthelmy S.D., Courvoisier T. J.-L., Gehrels, N., Soldi S., Tueller J., Wendt, G. 2007, *A&A*, 475, 827
- de Bruyn A.G. 1989, *A&A*, 226L, 13
- Bird A. J., Malizia A., Bazzano A. et al. 2007, *ApJS*, 170, 175
- De Rosa A. et al., 2008 accepted for publication in *A&A*
- Dickey J.M. & Lockman F.J. 1990, *ARA&A*, 28, 215
- Evans D.A., Worrall D.M., Hardcastle M.J., Kraft R.P. & Birkinshaw M. 2006, *ApJ*, 642, 96
- Fan J.H. & Zhang J.S. 2003, *A&A*, 407, 899
- Gliozzi M., Sambruna R.M., Eracleous M. 2003, *ApJ*, 584, 176

Table 3

Spectral Fit Results: $w_a g * w_a * (po+zga)$

Name	N_H (10^{22} cm^{-2})	Γ	E_{line} (keV)	σ (eV)	EW (eV)	C_1^A	C_2^B	χ^2 (dof)
QSO B0241+62	$0.23^{+0.08}_{-0.08}$	$1.65^{+0.07}_{-0.07}$	$6.40^{+0.06}_{-0.06}$	10f	85^{+43}_{-45}	$1.02^{+0.22}_{-0.18}$	$1.32^{+0.32}_{-0.26}$	227.1 (234)
B3 0309+411	-	$1.82^{+0.03}_{-0.03}$	$6.34^{+0.07}_{-0.09}$	10f	100^{+43}_{-50}	-	$4.65^{+2.11}_{-2.00}$	574.6 (603)
3C 111	$0.43^{+0.02}_{-0.02}$	$1.69^{+0.02}_{-0.02}$	$6.40^{+0.05}_{-0.05}$	10f	<30	$0.44^{+0.05}_{-0.04}$	$0.54^{+0.11}_{-0.10}$	1245.7 (1498)
IGR J13109-5552	$0.27^{+0.23}_{-0.27}$	$1.70^{+0.24}_{-0.22}$	-	-	-	-	$2.39^{+1.84}_{-0.99}$	41.2 (55)
3C 390.3	-	$1.74^{+0.01}_{-0.01}$	$6.44^{+0.02}_{-0.04}$	10f	71^{+8}_{-18}	$0.90^{+0.07}_{-0.07}$	$0.94^{+0.10}_{-0.11}$	2200.4 (2234)
4C 74.26	$0.12^{+0.01}_{-0.01}$	$1.73^{+0.02}_{-0.01}$	$6.44^{+0.05}_{-0.06}$	183^{+84}_{-65}	103^{+25}_{-25}	$0.54^{+0.09}_{-0.09}$	$0.87^{+0.23}_{-0.25}$	1992.0 (2060)
S5 2116+81	<0.19	$1.97^{+0.12}_{-0.12}$	-	-	-	$1.52^{+0.60}_{-0.44}$	$2.76^{+1.34}_{-0.85}$	89.1 (128)
IGR J21247+5058	$0.69^{+0.02}_{-0.02}$	$1.33^{+0.02}_{-0.01}$	$6.39^{+0.05}_{-0.08}$	10f	<30	$0.32^{+0.02}_{-0.02}$	$0.36^{+0.05}_{-0.02}$	2692.3 (2559)

A: cross-calibration constant between *XMM* and *BAT*; B: cross-calibration constant between *XMM* and *INTEGRAL/ISGRI*.

Table 3A

3C 390.3 Spectral Fits Results: $w_a g * (bb+po+zga)$

N_H (10^{22} cm^{-2})	Γ	kT (keV)	E_{line}^\ddagger (keV)	EW (eV)	C_1^A	C_2^B	χ^2 (dof)
-	$1.89^{+0.02}_{-0.02}$	$2.41^{+0.22}_{-0.17}$	$6.42^{+0.04}_{-0.05}$	49^{+9}_{-15}	$1.37^{+0.16}_{-0.15}$	$1.58^{+0.24}_{-0.21}$	1970.4 (2232)

‡ : line width fixed to 10 eV.

A: cross-calibration constant between *XMM* and *BAT*; B: cross-calibration constant between *XMM* and *INTEGRAL/ISGRI*.

Table 3B

IGR J21247+5058 Spectral Fit Results: $w_a g * pcfabs * pcfabs * (po+zga)$

Γ	N_H^1 (10^{22} cm^{-2})	cf_1	N_H^2 (10^{22} cm^{-2})	cf_2	E_{line}^\ddagger (keV)	EW (eV)	C_1^A	C_2^B	χ^2 (dof)
-	$10.81^{+1.88}_{-1.49}$	$0.38^{+0.03}_{-0.03}$	$1.08^{+0.16}_{-0.15}$	$0.86^{+0.04}_{-0.03}$	$6.39^{+0.07}_{-0.08}$	<30	$0.62^{+0.06}_{-0.05}$	$0.79^{+0.08}_{-0.06}$	2356.2 (2556)

‡ : line width fixed to 10 eV.

A: cross-calibration constant between *XMM* and *BAT*; B: cross-calibration constant between *XMM* and *INTEGRAL/ISGRI*.

Table 4

Spectral Fit Results: $w_a g * w_a * (cutoffpl+zga)$

Name	N_H (10^{22} cm^{-2})	Γ	E_{cut} (keV)	E_{line} (keV)	σ (eV)	EW (eV)	C_1^A	C_1^B	χ^2 (dof)	Prob. ‡
QSO B0241+61	$0.18^{+0.09}_{-0.09}$	$1.58^{+0.09}_{-0.09}$	>78	$6.40^{+0.07}_{-0.07}$	10f	80^{+41}_{-48}	$1.14^{+0.23}_{-0.21}$	$1.54^{+0.39}_{-0.34}$	222.9 (233)	96%
B3 0309+411	-	$1.80^{+0.02}_{-0.02}$	>43	$6.34^{+0.07}_{-0.09}$	10f	99^{+48}_{-47}	-	$6.75^{+3.81}_{-3.81}$	573.9 (602)	91%
3C 111	$0.42^{+0.02}_{-0.02}$	$1.65^{+0.03}_{-0.03}$	110^{+118}_{-40}	$6.40^{+0.05}_{-0.05}$	10f	<30	$0.56^{+0.09}_{-0.08}$	$0.74^{+0.19}_{-0.17}$	1234.2 (1497)	99.9%
IGR J13109-5552	<0.46	$1.55^{+0.31}_{-0.28}$	>58	-	-	-	-	$2.29^{+1.84}_{-0.99}$	39.8 (54)	83%
4C 74.26	$0.11^{+0.01}_{-0.01}$	$1.70^{+0.03}_{-0.03}$	>78	$6.44^{+0.05}_{-0.06}$	184^{+78}_{-66}	104^{+31}_{-26}	$0.63^{+0.16}_{-0.14}$	$1.09^{+0.44}_{-0.37}$	1989.9 (2059)	86%
S5 2116+81	<0.18	$1.95^{+0.14}_{-0.14}$	>81	-	-	-	$1.54^{+0.64}_{-0.44}$	$2.87^{+1.39}_{-1.04}$	89.2 (127)	-

A: cross-calibration constant between *XMM* and *BAT*; B: cross-calibration constant between *XMM* and *INTEGRAL/ISGRI*.

‡ : fit improvement with respect to table 3.

Table 4A

3C390.3 Spectral Fits Results: $w_a g * (bb+cutoffpl+zga)$

N_H (10^{22} cm^{-2})	Γ	kT (keV)	E_{cut} (keV)	E_{line}^\ddagger (keV)	EW (eV)	C_1^A	C_2^B	χ^2 (dof)	Prob. ‡
-	$1.89^{+0.02}_{-0.01}$	$2.41^{+0.21}_{-0.16}$	NC	$6.43^{+0.03}_{-0.04}$	48^{+9}_{-14}	$1.37^{+0.16}_{-0.15}$	$1.58^{+0.23}_{-0.11}$	1970.2 (2231)	37%

‡ : line width fixed to 10 eV.

A: cross-calibration constant between *XMM* and *BAT*; B: cross-calibration constant between *XMM* and *INTEGRAL/ISGRI*.

‡ : fit improvement with respect to table 3A.

Table 4B

IGR J21247+5058 Spectral Fit Results: $w_a g * pcfabs * pcfabs * (cutoffpl+zga)$

Γ	N_H^1 (10^{22} cm^{-2})	cf_1	N_H^2 (10^{22} cm^{-2})	cf_2	E_c (keV)	E_{line}^\ddagger (keV)	EW (eV)	C_1^A	C_2^B	χ^2 (dof)	Prob. ‡
-	$0.80^{+0.15}_{-0.17}$	$0.88^{+0.11}_{-0.05}$	$8.23^{+1.70}_{-2.05}$	$0.27^{+0.04}_{-0.05}$	80^{+100}_{-63}	$6.39^{+0.07}_{-0.08}$	<30	$0.65^{+0.05}_{-0.06}$	$0.86^{+0.07}_{-0.07}$	2276.8 (2555)	>99.9%

‡ : line width fixed to 10 eV.

A: cross-calibration constant between *XMM* and *BAT*; B: cross-calibration constant between *XMM* and *INTEGRAL/ISGRI*.

‡ : fit improvement with respect to table 3B.

Table 5
Spectral Fit Results: $w_a g * w_a * (\text{pexrav+zga})$, $0 \leq R \leq 2$, $E_c = 10000$

Name	N_H (10^{22} cm^{-2})	Γ	R	E_{line} (keV)	σ_{line} (eV)	EW (eV)	C_1^A	C_2^B	χ^2 (dof)	Prob. [†]
QSO B0241+61	$0.31^{+0.04}_{-0.10}$	$1.83^{+0.07}_{-0.15}$	>0.37	$6.40^{+0.08}_{-0.03}$	10f	67^{+40}_{-42}	$0.59^{+0.28}_{-0.11}$	$0.74^{+0.36}_{-0.16}$	224.1 (233)	92%
B3 0309+411	-	$1.92^{+0.03}_{-0.04}$	>1.20	$6.33^{+0.09}_{-0.10}$	10f	70^{+41}_{-43}	-	$2.42^{+1.06}_{-0.97}$	560.4 (602)	99.99%
3C 111	$0.48^{+0.03}_{-0.03}$	$1.78^{+0.05}_{-0.06}$	$1.06^{+0.63}_{-0.68}$	$6.40^{+0.07}_{-0.08}$	10f	<30	$0.30^{+0.07}_{-0.04}$	$0.35^{+0.11}_{-0.07}$	1238.5 (1497)	99.7%
IGR J13109-5552	$0.26^{+0.25}_{-0.25}$	$1.75^{+0.23}_{-0.25}$	>0.1	-	-	-	-	$1.30^{+2.69}_{-0.74}$	40.5 (54)	66%
4C 74.26	$0.16^{+0.02}_{-0.02}$	$1.84^{+0.05}_{-0.04}$	$1.30^{+0.67}_{-0.51}$	$6.45^{+0.04}_{-0.06}$	<186	51^{+37}_{-16}	$0.33^{+0.07}_{-0.06}$	$0.54^{+0.16}_{-0.17}$	1977.0 (2059)	99.99%
S5 2116+81	<0.22	$2.03^{+0.20}_{-0.16}$	>0.1	-	-	-	$1.10^{+0.73}_{-0.43}$	$1.97^{+1.51}_{-0.87}$	88.5 (127)	64%

A: cross-calibration constant between *XMM* and *BAT*; B: cross-calibration constant between *XMM* and *INTEGRAL/ISGRI*.
†: fit improvement with respect to table 3.

Table 5A
3C 390.3 Spectral Fits Results: $w_a g * w_a * (\text{bb+pexrav+zga})$, $0 \leq R \leq 2$, $E_c = 10000$

N_H (10^{22} cm^{-2})	Γ	kT (keV)	R	E_{line}^\ddagger (keV)	EW (eV)	C_1^A	C_2^B	χ^2 (dof)	Prob. [†]
-	$1.89^{+0.03}_{-0.02}$	$2.38^{+0.27}_{-0.22}$	$0.70^{+0.48}_{-0.59}$	$6.43^{+0.03}_{-0.04}$	44^{+10}_{-13}	$0.88^{+0.42}_{-0.13}$	$0.93^{+0.55}_{-0.22}$	1965.4 (2231)	98%

‡: line width fixed to 10 eV.
A: cross-calibration constant between *XMM* and *BAT*; B: cross-calibration constant between *XMM* and *INTEGRAL/ISGRI*.
†: fit improvement with respect to table 3A.

Table 5B
IGR J21247+5058 Spectral Fit Results: $w_a g * \text{pcfabs} * \text{pcfabs} * (\text{pexrav+zga})$, $0 \leq R \leq 2$, $E_c = 10000$

Γ	N_H^1 (10^{22} cm^{-2})	cf_1	N_H^2 (10^{22} cm^{-2})	cf_2	R	E_{line}^\ddagger (keV)	EW (eV)	C_1^A	C_2^B	χ^2 (dof)	Prob. [†]
$1.77^{+0.05}_{-0.05}$	$8.14^{+1.81}_{-1.69}$	$0.36^{+0.03}_{-0.04}$	$0.99^{+0.16}_{-0.18}$	$0.88^{+0.05}_{-0.03}$	$0.93^{+0.59}_{-0.45}$	$6.38^{+0.08}_{-0.08}$	<30	$0.41^{+0.08}_{-0.06}$	$0.50^{+0.10}_{-0.08}$	2341.7 (2555)	99.99%

‡: line width fixed to 10 eV.
A: cross-calibration constant between *XMM* and *BAT*; B: cross-calibration constant between *XMM* and *INTEGRAL/ISGRI*.
†: fit improvement with respect to table 3.

Table 6
Spectral Fit Results: $w_a g * w_a * (\text{pexrav+zga})$

Name	N_H (10^{22} cm^{-2})	Γ	R	E_c (keV)	EW [†] (eV)	C_1^A	C_2^B	χ^2 (dof)
QSO B0241+61	$0.21^{+0.15}_{-0.10}$	$1.64^{+0.22}_{-0.14}$	$0.56^{+0.82}_{-0.41}$	>86	73^{+44}_{-42}	$0.85^{+0.44}_{-0.32}$	$1.12^{+0.65}_{-0.48}$	222.2 (233)
B3 0309+411	-	$1.90^{+0.08}_{-0.08}$	$3.48^{+2.41}_{-1.58}$	35^{+91}_{-17}	59^{+42}_{-43}	-	$6.89^{+9.39}_{-3.90}$	554.2 (601)
3C 111	$0.46^{+0.03}_{-0.03}$	$1.73^{+0.06}_{-0.06}$	$0.85^{+0.58}_{-0.58}$	126^{+193}_{-50}	<30	$0.40^{+0.11}_{-0.08}$	$0.52^{+0.19}_{-0.13}$	1227.9 (1497)
3C 390.3	-	$1.89^{+0.03}_{-0.02}$	$0.60^{+0.60}_{-0.55}$	>300	41^{+12}_{-11}	$0.95^{+0.17}_{-0.25}$	$1.01^{+0.39}_{-0.30}$	1966.3 (2231)
4C 74.26	$0.14^{+0.02}_{-0.03}$	$1.79^{+0.06}_{-0.07}$	$1.22^{+0.65}_{-0.70}$	100^{+680}_{-52}	88^{+23}_{-20}	$0.95^{+0.25}_{-0.25}$	$1.01^{+0.39}_{-0.30}$	1976.0 (2060)
IGR J21247+5058	complex*	$1.48^{+0.06}_{-0.06}$	<0.21	79^{+23}_{-15}	<30	$0.65^{+0.05}_{-0.08}$	$0.86^{+0.08}_{-0.12}$	2276.7 (2555)

†: line parameters fixed at value obtained in table 3.
A: cross-calibration constant between *XMM* and *BAT*; B: cross-calibration constant between *XMM* and *INTEGRAL/ISGRI*.
*: $N_H^1 = 7.86^{+2.02}_{-1.66}$, $cf_1 = 0.27^{+0.04}_{-0.05}$; $N_H^2 = 0.77^{+0.18}_{-0.13}$, $cf_2 = 0.89^{+0.10}_{-0.06}$.

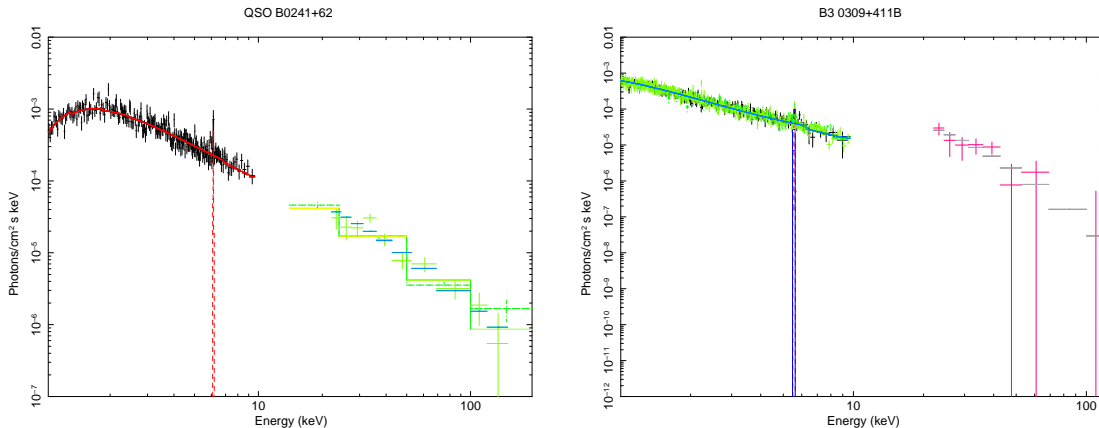


Figure 7. Table 6 model for QSO B0241+62 (left panel) and B3 0309+411 (right panel). The model is a cut-off power law absorbed both by Galactic and intrinsic column density reflected by neutral material plus a narrow Gaussian component describing the iron line.

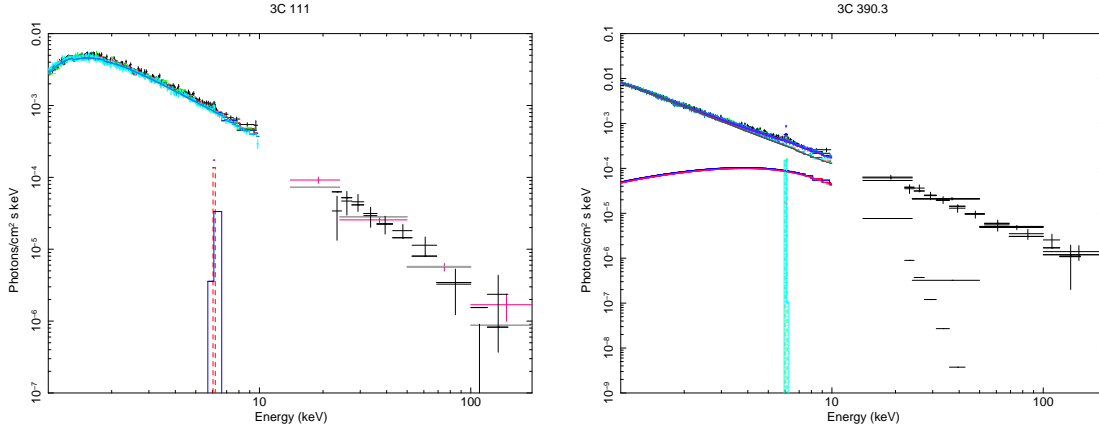


Figure 8. Table 6 model for 3C 111 (left panel) and 3C390.3 (right panel). The model is a cut-off power law absorbed both by Galactic and intrinsic column density reflected by neutral material plus a narrow Gaussian component describing the iron line.

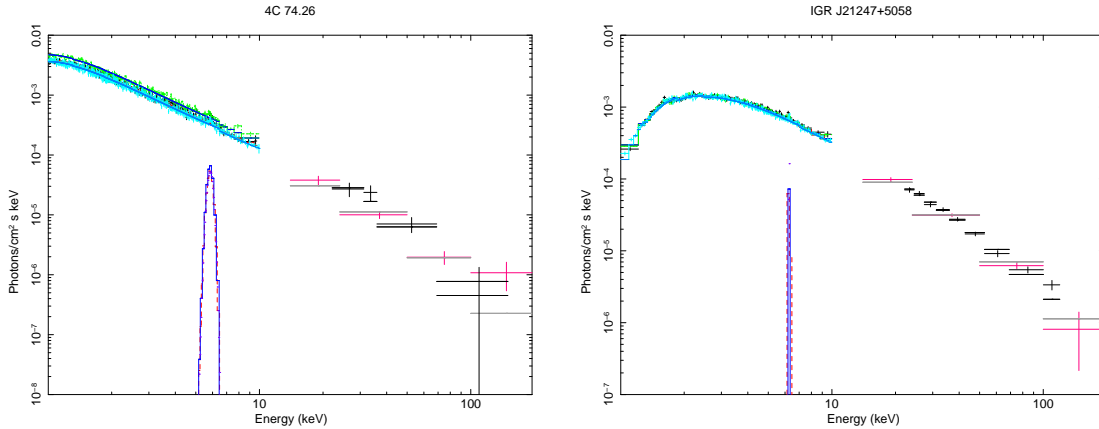


Figure 9. Table 6 model for 4C 74.26 (right panel) and IGR J21247+5058 (left panel). The model is a cut-off power law absorbed both by Galactic and intrinsic column density reflected by neutral material plus a narrow Gaussian component describing the iron line.

Grandi P., Guainazzi M., Haardt F., Maraschi L., Massaro E., Matt G., Piro L., Urry C. M. 1999, *A&A*, 343, 33
 Grandi P., Malaguti G. & Focchi M. 2006, *ApJ*, 642, 113
 Goldwurm A., David P., Foschini L. et al. 2003, *A&A*, 411, 223
 Hardcastle M. J. & Croston, J. H. 2005, *MNRAS*, 363, 649
 Hill J.E., Burrows D. N. Nousek J.A. et al. 2004, *SPIE*, 5165, 217
 Ho L.C. & Peng C.Y. 2001, *ApJ*, 555, 650 2003, *ApJ*, 126, 153
 Ishwara-Chandra C. H. & Saikia D. J. 1999, *MNRAS*, 309,100
 Kadler M., Ros E., Kerp J., Kovalev Y.Y., Zensus J.A. 2004, *Proc. 7th European VLBI Network Symposium* Edited by R. Bachiller, F. Colomer, J.-F.; Desmurs, and P. de Vicente, 23
 Kellermann K.I., Sramek R., Schmidt M., Shaffer D.B., Green R. 1989, *AJ*, 98, 1195
 Kharb P., O’Dea C.P., Baum S.A. et al. 2006, *ApJ*, 652, 177
 Lal D.V., Shastri P. & Gabuzda D. C. 2004, *A&A*, 425, 99
 Landi R., De Rosa A. Dean A.J. et al. 2007, *MNRAS*, 380, 926
 Larsson J., Fabian A.C., Ballantyne D.R & Miniutti G. astro-ph 0805.3603
 Lebrun F., Leray J.P., Lavocat P. et al. 2003 *A&A*, 411, 141
 Lewis K.T., Eracleous M., Gliozzi M., Sambruna R.M., Mushotzky R.F. 2005, *ApJ*, 622, 816
 Malizia A., Bassani L., Capalbi M. et al. 2003, *A&A*, 406, 105
 Malizia et al. 2008, private communication
 Maraschi L. & Haardt F. 1997, *ASPC*, 121, 101
 Masetti N., Landi R., Pretorius M.L. et al. 2007, *A&A* 470, 331

Masetti N., Mason E., Morelli L. et al. 2008, *A&A*, 482, 113
 Matt G. 2001, *AIPC*, 599, 209
 Matt G., Bianchi S., De Rosa A., Grandi P. & Perola G.C. 2006, *A&A*, 445,451
 Mattson B.J., Weaver K.A. and Reynolds C.S. 2007 *ApJ*, 664,101
 Merloni A., Malzac J., Fabian A.C. & Ross R.R. 2006, *MNRAS*, 370, 1699
 Miller L., Peacock J.A. & Mead A.R.G. 1990, *MNRAS*, 244, 207
 Molina M., Malizia A., Bassani L., Bird A.J., Dean A.J., Landi R. et al. 2006, *MNRAS*, 371, 821
 Molina M., Giroletti M., Malizia A. et al. 2007, *MNRAS*, 382, 937
 Murphy T., Mauch T., Green A., Hunstead R. W., Piestrzynska B., Kels A.P., Sztajer P. 2007, *MNRAS*, 382, 382
 Mushotzky, R. F., Done, C., Pounds, K., A. 1993, *ARA&A*, 31, 717
 Panessa F., Bassani L., De Rosa A. et al. 2008, *A&A*, 483, 151
 Perola G. C., Matt G., Cappi M., Fiore F., Guainazzi M., Maraschi L., Petrucci P.O., Piro L. 2002, *A&A*, 389, 802
 Petrucci P.O., Haardt F., Maraschi L. et al. 2001, *ApJ*, 556, 716
 Riley J.M., Warner P.J., Rawlings S., Saunder R., Pooley G.G., Eales S.A. 1988, *MNRAS*, 236, 13
 Risaliti G. 2002 *A&A*, 386, 379
 Sambruna R.M., Eracleous M., Mushotzky R.F. 1999, *ApJ*, 526,

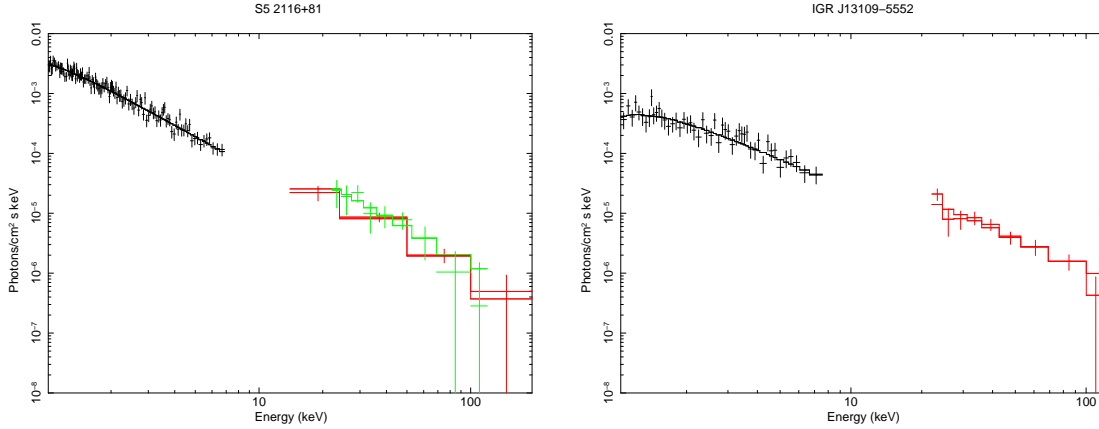


Figure 10. Table 3 model for S5 2116+81 (left panel) and IGR J13109-5552 (right panel). The model is a simple power law, absorbed both by Galactic and intrinsic column densities.

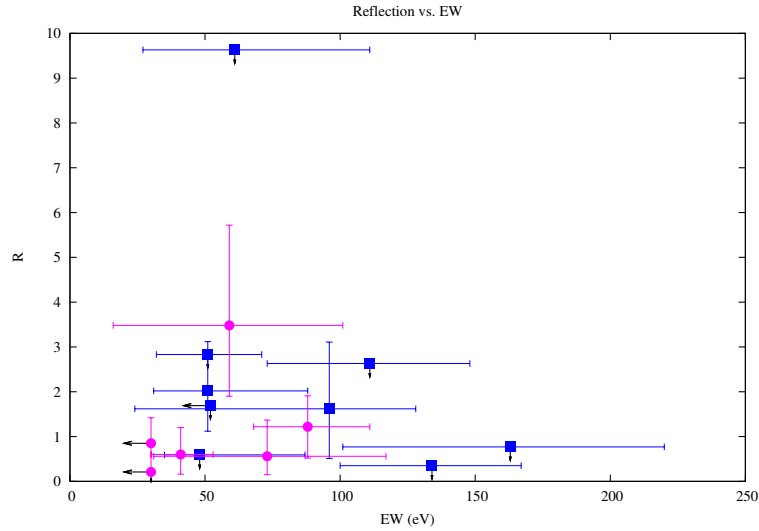


Figure 11. Reflection fraction vs. EW for the sample analysed here and the sources presented in Panessa et al. (2008). Blue squares are radio quiet sources, while radio loud sources are represented by magenta circles. Arrows represent upper or lower limits on the parameter values.

60

Sambruna R. M., Reeves J. N. & Braitto, V. 2007 ApJ, 665, 1030
 Strüder L., Briel U., Dennerl K. et al. 2001, A&A, 365L, 18
 Turner M. J. L., Abbey A., Arnaud, M. et al. 2001, A&A, 365L, 27
 Tzanetakis A., Spencer R.E., Masson C.R., Baldwin J.E. 1978, MNRAS, 185, 63
 Ubertini P., Lebrun F., Di Cocco G. et al. 2003, A&A 411, 131
 Ulvestad J.S. & Wilson A.S., 1986, MNRAS, 218, 711
 Unger V., Nguyen Q.R., Mauron N., Brillet J. 1985 A&A, 146, 123
 Vollmer B., Davoust E., Dubois P. et al. 2005, A&A, 436, 757
 Winter L.M., Mushotzky R.F., Tueller J. & Markwardt C. 2008, ApJ, 674, 686
 Zamfir S., Sulentic J.W. & Marziani P. 2008, astro-ph 0804.0788